Attosecond time–energy structure of X-ray free-electron laser pulses

N. Hartmann[1,2,17]*, G. Hartmann[3,4], R. Heider[5], M. S. Wagner[5], M. Ilchen[1,6,7], J. Buck [3,6],
A. O. Lindahl[1,8,9], C. Benko[10], J. Grünert [6], J. Krzywinski[1], J. Liu[6], A. A. Lutman[1], A. Marinelli[1],
T. Maxwell [1], A. A. Miahnahri[1], S. P. Moeller[1], M. Planas[6], J. Robinson[1], A. K. Kazansky[11,12,13],
N. M. Kabachnik[6,14], J. Viefhaus[3], T. Feurer[2], R. Kienberger[5,15], R. N. Coffee[1,7] and W. Helml [1,5,16]*

The time–energy information of ultrashort X-ray free-electron laser pulses generated by the Linac Coherent Light Source is measured with attosecond resolution via angular streaking of neon 1s photoelectrons. The X-ray pulses promote electrons from the neon core level into an ionization continuum, where they are dressed with the electric field of a circularly polarized infrared laser. This induces characteristic modulations of the resulting photoelectron energy and angular distribution. From these modulations we recover the single-shot attosecond intensity structure and chirp of arbitrary X-ray pulses based on self-amplified spontaneous emission, which have eluded direct measurement so far. We characterize individual attosecond pulses, including their instantaneous frequency, and identify double pulses with well-defined delays and spectral properties, thus paving the way for X-ray pump/X-ray probe attosecond free-electron laser science.

Attosecond science based on high-harmonic generation (HHG) of optical lasers[1–3] has led to new insights into fundamental quantum-mechanical dynamics. It provides previously inaccessible knowledge and control of processes such as atomic electron tunnelling[4] and photoemission delay[5], transport delay times in solids[6,7], coherent electron dynamics in both atoms[8] and molecules[9], proton dynamics in molecules[10] and light-field-controlled reversible phase transitions in dielectrics[11]. At the same time, novel ultrabright X-ray free-electron laser (XFEL) facilities have been developed[12–17], which have opened the door to high-intensity X-ray experiments in the physical[18], chemical[19], life[20] and material sciences[21], with implications to state-of-the-art technology and modern medicine. In spite of pioneering results of coherent control with seeded FELs[22], most of these XFEL sources rely on the principle of self-amplification of spontaneous emission (SASE) by relativistic electrons in the periodically varying magnetic field of an undulator[23]. This produces ultrashort bursts of X-rays with energies of up to tens of millijoules at wavelengths down to the ångström level, corresponding to approximately 10^{12} photons per pulse in the photon energy range from 0.5 keV to 8 keV. Thus, XFELs extend ultrafast science to the X-ray regime, complementing state-of-the-art HHG sources, which have only just recently demonstrated unprecedented 53-attosecond pulses at the carbon K-edge (284 eV)[24], albeit at a comparatively low flux of 10^5 photons per pulse. However, combining attosecond temporal resolution with high-brilliance sub-nanometre-scale coherent X-rays at XFELs has eluded researchers, largely due to the stochastic nature of their generation and an according lack of knowledge about the temporal structure and instantaneous frequency of individual SASE pulses, which can up to now not be provided by other established methods for characterization[25–29].

Here, we report the measurement of attosecond time–energy information of individual XFEL pulses through angular streaking of X-ray-generated photoelectrons with a circularly polarized infrared (IR) laser pulse, where the time axis is mapped onto the angular axis. From this, we reconstruct the streaking field amplitude and phase as well as the intensity structure and chirp of the XFEL pulses on a single-shot basis with attosecond resolution. We find that the reconstructed substructure of the XFEL pulses is consistent with lower-resolution, indirect X band transverse cavity (XTCAV) measurements[28] as well as with theoretical predictions of the SASE process[30]. Not only confirming fundamental aspects of X-ray pulse generation in XFELs, this allows for sophisticated sorting of experimental data. We detect individual attosecond pulses, including their instantaneous frequency, and identify double attosecond X-ray pulses with a range of well-defined relative delays to recover attosecond-resolved X-ray pump/X-ray probe results. Together with recent proposals for attosecond X-ray pulse generation at XFELs[31–33] in combination with new XFEL pulse-shaping techniques[34–36] and synchronized IR lasers, this brings the full arsenal of lab-based attoscience to the high-intensity regime of XFELs.

Results

Experimental set-up—angular streaking spectroscopy. Previous streaking measurements of XFEL pulses[37–39] used a linearly polarized streaking field to encode their temporal profile onto the kinetic energy of photoelectrons. Depending on the amplitude and phase of

the streaking field at the time of ionization, the photoelectrons are either accelerated or decelerated, and the corresponding momentum change is measured with a time-of-flight (TOF) detector. For such conventional linear streaking, one would ideally overlap the X-ray pulse with the largest slope of the streaking field for the best possible time resolution. However, the exact temporal overlap with this streaking ramp is not guaranteed for every X-ray shot due to inherent arrival time jitter[40,41] with respect to the streaking laser pulse, which leads to ambiguities in the interpretation[37]. As a result, linear streaking has so far not demonstrated sufficient capability to resolve the complex temporal substructure and instantaneous frequency of SASE pulses. These limitations can be overcome by encoding the time information into the energy-resolved angular distribution of circularly streaked photoelectrons, which has very recently also been investigated theoretically with a rotating terahertz field for studying the temporal parameters of XFEL pulses[42,43].

Towards this end, we performed angular streaking measurements at the Atomic, Molecular and Optical Science (AMO) instrument of the Linac Coherent Light Source (LCLS), achieving the attosecond time–energy characterization of XFEL pulses. Ultrashort X-ray pulses with an estimated average duration of ~7 fs (full-width at half-maximum (FWHM)) or ~3 fs (root-mean-square (r.m.s.)) and a photon energy of 1,180 eV non-resonantly ionize a dilute target of neon atoms. The emitted photoelectrons from the neon core shell ($E_{bind} = 870$ eV) with a mean kinetic energy of $E_{kin} = (1,180 - 870)$ eV $= 310$ eV are detected by an angular array of 16 TOF spectrometers[44,45] that are evenly distributed around the plane perpendicular to the X-ray beam propagation direction (Fig. 1). Ne $1s$ photoelectrons exhibit a dipole emission pattern along the horizontal linear X-ray polarization due to the spherical symmetry of the initial orbital. The time-dependent yield of photoelectrons is a replica of the temporal intensity profile of the X-ray pulse[46].

We capitalize on the continuously rotating electric field of a close-to-circularly polarized infrared streaking laser such that the amplitude of the field is nearly constant within one rotation, sweeping the angle of the streaking direction over a full cycle[47]. The rotating field can be thought of as the hand of a clock whose face is given by the oscillation period of the streaking laser. The time for one revolution of this so-called attoclock[48] is set by the streaking wavelength, $\lambda = 10.6$ μm, corresponding to a ~35 fs period of rotation. This period was chosen to be longer than the expected X-ray pulse duration to avoid ambiguity from multiple revolutions of the clock within one XFEL pulse.

Figure 1 illustrates the principle of angular streaking. The kinetic energy of photoelectrons $W(W_0, \theta, t_i)$ is a function of observation

angle θ and initial electron energy W_0, which is offset by the streaking kick σ in the direction of the vector potential at the time of ionization t_i (refs [49–51]):

$$W(W_0, \theta, t_i) \propto W_0 + \sigma \cos\left(\theta - 2\pi \frac{ct_i}{\lambda}\right)$$

Here, c is the speed of light. The spectral bandwidth and chirp of the X-rays determine the initial electron energy distribution, and the photoelectron counts are directly proportional to the momentary X-ray intensity. We decode these quantities of interest from the single-shot angular streaking data with an iterative projection algorithm that decomposes the streaking trace into a time–energy representation of the X-ray pulse. The algorithm, as explained in detail in the Supplementary Methods, has been thoroughly tested on multiple shots and parameter ranges and has been found to be very robust with respect to uncertainties on the order of the measurement error as well as to lead to unique solutions even in the presence of noise. Comparison with a full quantum-mechanical simulation described in the Supplementary Discussion further corroborates the validity of the applied approach.

Attosecond-scale SASE XFEL pulse time–energy distribution. Shot-to-shot fluctuations in the electron accelerator for the XFEL alter the electron bunch phase space, and therefore the resulting X-ray time–energy distribution. Furthermore, built up from shot noise, the typical substructure of a SASE X-ray pulse is fairly complex owing to this stochastic origin of the SASE process. The spontaneous emission of synchrotron radiation in the undulator and the interaction of the electromagnetic field back on the electrons lead to small-scale order in the lasing electron bunch, limited by the longitudinal coherence length[30,52]. Subsections of the electron bunch therefore have no fixed phase relationship, and act as independent radiation sources. This leads to temporally coherent spikes in the emitted X-ray pulses, while the electric field is uncorrelated between these spikes. Theoretical calculations for the XFEL predict pulse trains of multiple coherent SASE spikes[53] whose number, intensities, durations, intrinsic chirps and positions within the X-ray pulse are random from shot to shot.

The measured temporal substructure of XFEL pulses (Fig. 2a–c) clearly shows the expected series of random pulse shapes and variation in instantaneous frequency. We observe that the number of SASE spikes changes considerably from shot to shot as well. This provides crucial information not just for time-resolved experiments
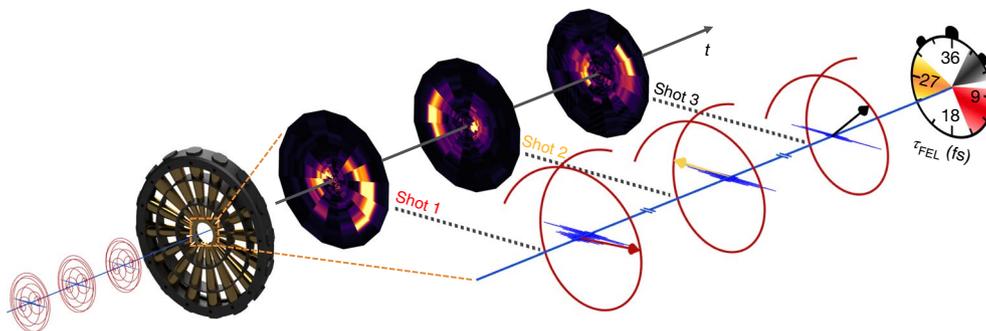

Fig. 1 | Angular streaking resolves the X-ray pulse structure via angle-dependent kinetic energy changes of photoelectrons. X-ray pulses ionize the target gas in the centre of the detector. The concomitant rotating IR laser field modifies the kinetic energy of the photoelectrons depending on their ionization time. Three individual X-ray pulses, denominated as shots 1, 2 and 3, overlap in the detection area (dashed orange rectangle, magnified picture on the right) with three IR pulses at different phases of their circularly polarized field and generate clearly distinguishable photoelectron time–energy distributions, shown as false colour polar plots of experimental data. In these plots, the intensity is proportional to the number of photoelectrons, the distance from the centre represents the kinetic energy of the photoelectrons, and the angle along the circle corresponds to the IR phase during photoionization by the X-ray pulse. The intensity structure and pulse duration (τ_{FEL}) of each X-ray pulse can be read from these distributions, similar to reading from a clock face.
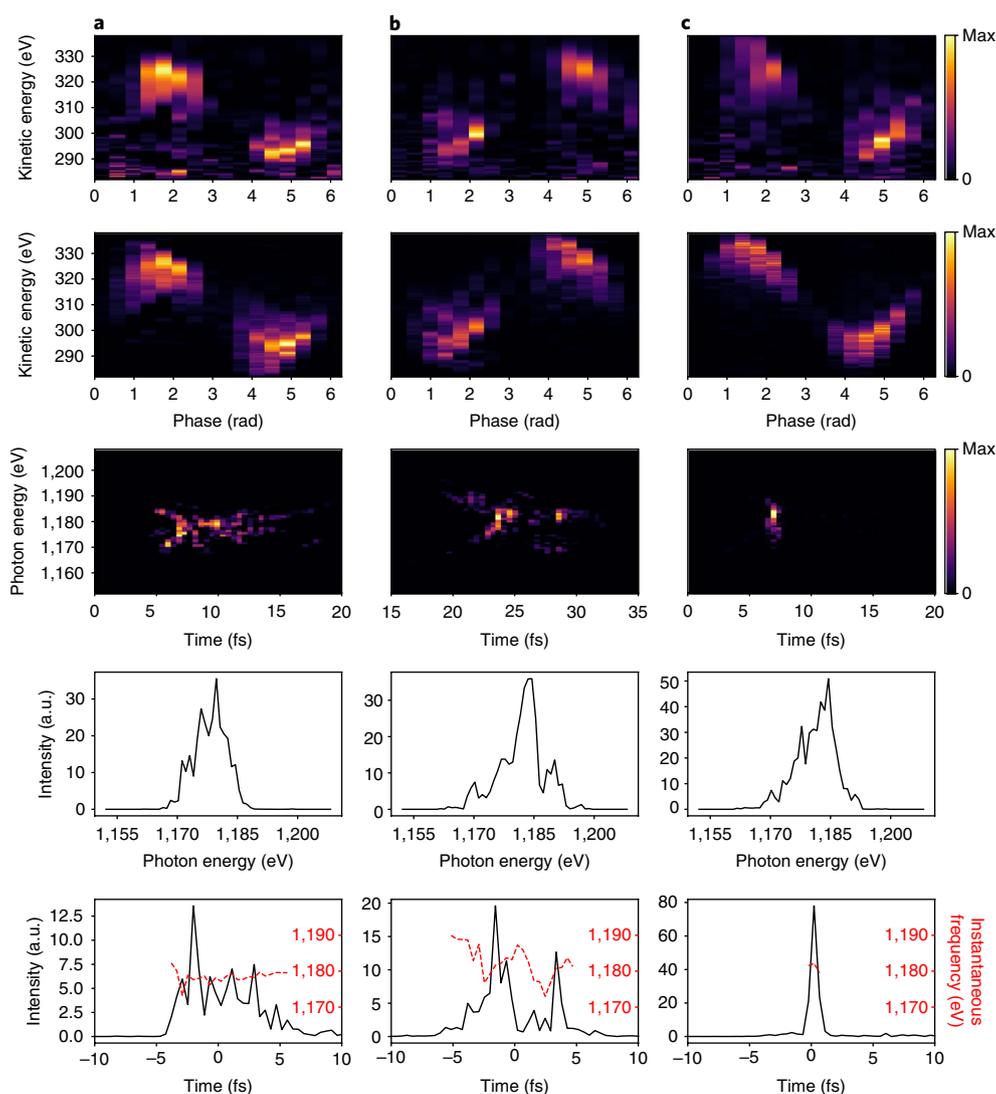
Fig. 2 | X-ray pulse time–energy characterization of three exemplary SASE XFEL shots. a–c, From top to bottom: angularly streaked Ne 1s photoelectron spectra, reconstructed photoelectron spectra, the reconstructed X-ray time–energy distributions (spectrograms), X-ray spectra and temporal profiles of three random X-ray shots **a**, **b** and **c**. The reconstruction is performed on a grid with 0.44 fs temporal resolution. The spectrograms in the third row clearly show overall residual chirp for shots **a** and **b**, while the single-spike shot **c** seems nearly fully compressed. This is also evident in more detail from the progression of the instantaneous frequency in the last row, which elicits broad variation and a non-monotonic slope across the main spikes in **a** and **b**, in contrast to shot **c** with a nearly flat shape of the instantaneous frequency curve. The spectral bandwidth is similar for all three shots, ranging between 6 eV and 10 eV FWHM. The XFEL pulse energies for the three shots are 36.5 μJ, 39.5 μJ and 40 μJ for **a**, **b** and **c**, respectively, underscoring the measurement robustness even for low X-ray pulse energies.

on the femtosecond to attosecond timescale, but also for any study of nonlinear processes relying on the precise knowledge of X-ray peak intensities. The presence of individual pulses with sub-femtosecond duration in our data also corroborates the feasibility of attosecond XFEL pulse generation and pulse-shaping schemes, as proposed in refs [32–34].

We derive the instantaneous frequency $\omega_x(t)$ for each X-ray pulse, defined as the centre of gravity for each slice of time in the time–energy distribution, which is the temporal derivative of the phase (as explained above, the temporal phase for a SASE pulse is only piece-wise defined and might exhibit discontinuities between the spikes) and gives access to the chirp of the X-ray pulse. This information can be used to give direct feedback on the compression settings for the electron bunches, since an overall linear chirp of the X-ray pulse partly derives from an uncompensated energy chirp of the electron bunch in the undulator [54]. Even more importantly, it

renders possible highly precise time–energy-resolved experiments at XFELs by distinguishing a shift in the X-ray pulse central frequency from intensity fluctuations. This allows one, for example, to unambiguously discern differential cross-section changes accompanying the X-ray excitation process or track specific dynamic potential energy surfaces during chemical reactions.

Attosecond XFEL double pulses for X-ray pump/probe measurements. The angular streaking results show that pulse durations vary significantly despite the fixed machine settings (Fig. 3a). These X-ray pulses were generated with a slotted emittance spoiler [55], resulting in a mean energy of 64 μJ or 3.4×10^{11} photons per pulse and an average pulse duration of 2.1 fs (r.m.s.). Simultaneously recorded XTCAV measurements [28] of the spent electron bunch corroborate these results (see also the Supplementary Discussion). The observation of X-ray pulses consisting of a single coherent SASE spike
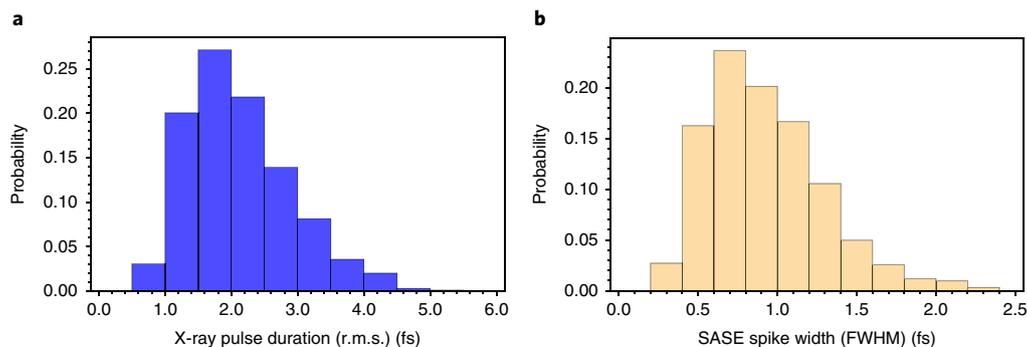
Fig. 3 | X-ray pulse statistics. a, Histogram of the total X-ray pulse durations (r.m.s.) with an average of 2.1 fs. **b**, Individual SASE spike durations (FWHM) obtained by fitting multiple Gaussians to the X-ray pulse substructure. The measured SASE spike duration is on average 800 as for this 1,180 eV photon energy. As expected for stochastic pulses based on the SASE process, we detect no obvious correlation between the durations of the individual SASE spikes and the number of spikes in a single XFEL pulse.

has been reported earlier[37], but their exact durations could not be unambiguously quantified. Here, we confirm the existence of single-spike pulses of sub-femtosecond durations (compare Fig. 3b). We find pulse lengths (FWHM) mainly ranging from 1.5 fs down to 500 as for the shortest observed single SASE-spike pulses in our dataset, like the one shown in Fig. 2c.

For investigations of correlation dynamics on the attosecond timescale, the development of an X-ray attosecond pump/probe set-up with variable delay and sufficient pulse intensity has been a long-standing goal. Our measurements demonstrate that this research avenue is already within reach of current XFELs thanks to the now-accessible unique properties of SASE pulses. Scanning our data for X-ray pulses with two sub-femtosecond spikes of approximately equal amplitude allows us to identify shots that are candidates for an X-ray pump/probe experiment. In Fig. 4 we show the resulting 3D intensity map of a delay range scan from 1.0 fs to 2.3 fs. Four exemplary shots are highlighted in panel b, each consisting of two ~800 as pulses with variable relative delay. Even in the current mode of FEL
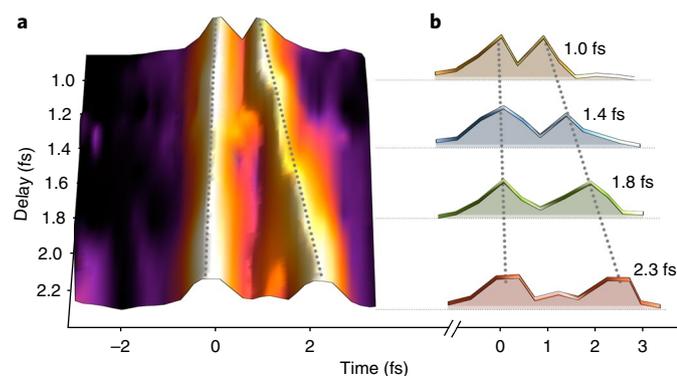
operation that was not optimized for double pulses, we detect 332 shots that contain attosecond double pulses of approximately equal ~30 μJ individual sub-pulse energy, each representing a full single-shot measurement at a given relative delay. Thus, the scheme makes attosecond double-pulse identification an ideal tool that enables attosecond-scale X-ray pump/X-ray probe science, opening the door to atom-specific electron–electron correlation experiments at the natural timescale of electron motion at XFELs.

Discussion

Besides characterizing individual SASE XFEL pulses on an attosecond timescale, we note that angular streaking can simultaneously measure the relative X-ray arrival time with few-femtosecond resolution (see Supplementary Discussion). Beyond that, a carrier–envelope phase-stabilized streaking field could deliver an arrival time resolution also at the attosecond level. The arrival time measurement described in the Supplementary Information could be used to identify the particular cycle of the streaking field. Then the recorded photoelectron streaking angle in the detector frame would provide the precise attosecond arrival time.

Demonstrated here for soft X-rays, this measurement also scales to hard X-rays, with their accompanying even shorter SASE spike durations. Changing the target gas, and hence the absorption edges to the required higher X-ray energy range, while at the same time decreasing the streaking wavelength allows a straightforward adaptation of the set-up to the specific needs of hard X-ray pulse characterization[56]. For example, substituting the 10.6 μm-wavelength laser with a standard 1,064 nm source, which is planned to be readily available at LCLS-II at a suitable repetition rate, the resolution is easily enhanced from 500 as to 50 as, simply by using a 10 times shorter wavelength for the streaking laser.

The angular streaking method requires minimal X-ray pulse energy with near-unity X-ray transmission. It is therefore ideally suited for single-shot X-ray pulse tagging in parallel with independently ongoing experiments, which allows for post-selection of specific pulse durations and photon energies, identification of isolated attosecond pulses, or the detection and delay-sorting of double spikes for attosecond pump/probe experiments. Finally, we note that TOF spectrometers as used here are applicable to high-repetition rate FELs such as the 100 kHz–1 MHz European XFEL and LCLS-II. The high repetition rate compensates the potentially low fraction of selected shots, while the sorting simultaneously alleviates the need for full-rate detector and data systems. Thus, angular streaking sets the stage for advanced X-ray pump/probe experiments, enabling site-specific, time-and-energy-resolved measurements on the natural timescale of electronic motion.

Fig. 4 | Attosecond X-ray double pulses from an XFEL. a,b, We identify double-spike pulses with variable temporal separation, showing four exemplary delay steps between 1.0 fs and 2.3 fs in **b**. The individual spikes have a duration of 600–800 as and a pulse energy of approximately 30 μJ each. These carefully selected attosecond double pulses amount to more than 0.3% of all shots in the evaluated dataset. In **a**, we plot a delay-sorted three-dimensional scan image of attosecond X-ray double pulses, defining the accessible delays for attosecond X-ray pump/probe measurements in our run. The temporal resolution for defining these delays is set to 0.2 fs. By changing the overall XFEL pulse duration, one can statistically syntonize to different delay ranges.

Methods

Methods, including statements of data availability and any associated accession codes and references, are available at https://doi.org/10.1038/s41566-018-0107-6.

References

1. Hentschel, M. et al. Attosecond metrology. *Nature* **414**, 509–513 (2001).
2. Krausz, F. & Stockman, M. I. Attosecond metrology: from electron capture to future signal processing. *Nat. Photon.* **8**, 205–213 (2014).
3. Drescher, M. X-ray pulses approaching the attosecond frontier. *Science* **291**, 1923–1927 (2001).
4. Eckle, P. et al. Attosecond ionization and tunneling delay time measurements in helium. *Science* **322**, 1525–1529 (2008).
5. Schultze, M. et al. Delay in photoemission. *Science* **328**, 1658–1662 (2010).
6. Cavalieri, A. L. et al. Attosecond spectroscopy in condensed matter. *Nature* **449**, 1029–1032 (2007).
7. Neppl, S. et al. Direct observation of electron propagation and dielectric screening on the atomic length scale. *Nature* **517**, 342–346 (2015).
8. Goulielmakis, E. et al. Real-time observation of valence electron motion. *Nature* **466**, 739–743 (2010).
9. Kraus, P. M. et al. Measurement and laser control of attosecond charge migration in ionized iodoacetylene. *Science* **350**, 790–795 (2015).
10. Baker, S. et al. Probing proton dynamics in molecules on an attosecond time scale. *Science* **312**, 424–427 (2006).
11. Schultze, M. et al. Controlling dielectrics with the electric field of light. *Nature* **493**, 75–78 (2014).
12. Emma, P. et al. First lasing and operation of an ångstrom-wavelength free-electron laser. *Nat. Photon.* **4**, 641–647 (2010).
13. Ishikawa, T. et al. A compact X-ray free-electron laser emitting in the sub-ångström region. *Nat. Photon.* **6**, 540–544 (2012).
14. Allaria, E. et al. Two-stage seeded soft-X-ray free-electron laser. *Nat. Photon.* **7**, 913–918 (2013).
15. Kang, H. -S. et al. Hard X-ray free-electron laser with femtosecond-scale timing jitter. *Nat. Photon.* **11**, 708–713 (2017).
16. Altarelli, M. The European X-ray free-electron laser facility in Hamburg. *Nucl. Instrum. Methods Phys. Res. Sect. B* **269**, 2845–2849 (2011).
17. Milne, C. et al. SwissFEL: The Swiss X-ray Free Electron Laser. *Appl. Sci.* **7**, 720 (2017).
18. Young, L. et al. Femtosecond electronic response of atoms to ultra-intense X-rays. *Nature* **466**, 56–61 (2010).
19. Zhang, W. et al. Tracking excited-state charge and spin dynamics in iron coordination complexes. *Nature* **509**, 345–348 (2014).
20. Seibert, M. M. et al. Single mimivirus particles intercepted and imaged with an X-ray laser. *Nature* **470**, 78–81 (2011).
21. Milathianaki, D. et al. Femtosecond visualization of lattice dynamics in shock-compressed matter. *Science* **342**, 220–223 (2013).
22. Prince, K. C. et al. Coherent control with a short-wavelength free-electron laser. *Nat. Photon.* **10**, 176–179 (2016).
23. Milton, S. V. et al. Exponential gain and saturation of a self-amplified spontaneous emission free-electron laser. *Science* **292**, 2037–2041 (2001).
24. Li, J. et al. 53-attosecond X-ray pulses reach the carbon K-edge. *Nat. Commun.* **8**, 186 (2017).
25. Lutman, A. et al. Femtosecond X-ray free electron laser pulse duration measurement from spectral correlation function. *Phys. Rev. ST Accel. Beams* **15**, 030705 (2012).
26. Inubushi, Y. et al. Determination of the pulse duration of an X-ray free electron laser using highly resolved single-shot spectra. *Phys. Rev. Lett.* **109**, 144801 (2012).
27. Ding, Y. et al. Femtosecond X-ray pulse characterization in free-electron lasers using a cross-correlation technique. *Phys. Rev. Lett.* **109**, 254802 (2012).
28. Behrens, C. et al. Few-femtosecond time-resolved measurements of X-ray free-electron lasers. *Nat. Commun.* **5**, 3762 (2014).
29. Sanchez-Gonzalez, A. et al. Accurate prediction of X-ray pulse properties from a free-electron laser using machine learning. *Nat. Commun.* **8**, 15461 (2017).
30. Krinsky, S. & Gluckstern, R. Analysis of statistical correlations and intensity spiking in the self-amplified spontaneous-emission free-electron laser. *Phys. Rev. ST Accel. Beams* **6**, 050701 (2003).
31. Zholents, A. & Fawley, W. Proposal for intense attosecond radiation from an X-ray free-electron laser. *Phys. Rev. Lett.* **92**, 224801 (2004).
32. Kumar, S., Kang, H.-S. & Kim, D. E. Tailoring the amplification of attosecond pulse through detuned X-ray FEL undulator. *Opt. Express* **23**, 2808–2818 (2015).
33. Prat, E. & Reiche, S. Simple method to generate terawatt-attosecond X-ray free-electron-laser pulses. *Phys. Rev. Lett.* **114**, 244801 (2015).
34. Marinelli, A. et al. Optical shaping of X-ray free-electron lasers. *Phys. Rev. Lett.* **116**, 254801 (2016).
35. Lutman, A. A. et al. Fresh-slice multicolour X-ray free-electron lasers. *Nat. Photon* **10**, 745–750 (2016).
36. Huang, S. et al. Generating single-spike hard X-ray pulses with nonlinear bunch compression in free-electron lasers. *Phys. Rev. Lett.* **119**, 154801 (2017).
37. Helml, W. et al. Measuring the temporal structure of few-femtosecond free-electron laser X-ray pulses directly in the time domain. *Nat. Photon.* **8**, 950–957 (2014).
38. Düsterer, S. et al. Femtosecond x-ray pulse length characterization at the Linac Coherent Light Source free-electron laser. *New J. Phys.* **13**, 093024 (2011).
39. Grguraš, I. et al. Ultrafast X-ray pulse characterization at free-electron lasers. *Nat. Photon* **6**, 852–857 (2012).
40. Hartmann, N. et al. Sub-femtosecond precision measurement of relative X-ray arrival time for free-electron lasers. *Nat. Photon.* **8**, 706–709 (2014).
41. Bionta, M. R. et al. Spectral encoding method for measuring the relative arrival time between X-ray/optical pulses. *Rev. Sci. Instrum* **85**, 083116 (2014).
42. Kazansky, A. K., Bozhevolnov, A. V., Sazhina, I. P. & Kabachnik, N. M. Interference effects in angular streaking with a rotating terahertz field. *Phys. Rev. A* **93**, 013407 (2016).
43. Kazansky, A. K., Sazhina, I. P., Nosik, V. L. & Kabachnik, N. M. Angular streaking and sideband formation in rotating terahertz and far-infrared fields. *J. Phys. B* **50**, 105601 (2017).
44. Allaria, E. et al. Control of the polarization of a vacuum-ultraviolet, high-gain, free-electron laser. *Phys. Rev. X* **4**, 041040 (2014).
45. Lutman, A. A. et al. Polarization control in an X-ray free-electron laser. *Nat. Photon.* **10**, 468–472 (2016).
46. Gagnon, J. & Yakovlev, V. S. The direct evaluation of attosecond chirp from a streaking measurement. *Appl. Phys. B* **103**, 303–309 (2011).
47. Constant, E., Taranukhin, V., Stolow, A. & Corkum, P. Methods for the measurement of the duration of high-harmonic pulses. *Phys. Rev. A* **56**, 3870–3878 (1997).
48. Eckle, P. et al. Attosecond angular streaking. *Nat. Phys.* **4**, 565–570 (2008).
49. Itatani, J. et al. Attosecond streak camera. *Phys. Rev. Lett.* **88**, 173903 (2002).
50. Kienberger, R. et al. Atomic transient recorder. *Nature* **427**, 817–821 (2004).
51. Kazansky, A. K., Sazhina, I. P. & Kabachnik, N. M. Angle-resolved electron spectra in short-pulse two-color XUV+IR photoionization of atoms. *Phys. Rev. A* **82**, 033420 (2010).
52. Behrens, C. et al. Constraints on photon pulse duration from longitudinal electron beam diagnostics at a soft x-ray free-electron laser. *Phys. Rev. ST Accel. Beams* **15**, 030707 (2012).
53. Pellegrini, C., Marinelli, A. & Reiche, S. The physics of x-ray free-electron lasers. *Rev. Mod. Phys.* **88**, 015006 (2016).
54. Li, Y., Lewellen, J., Huang, Z., Sajaev, V. & Milton, S. V. Time-resolved phase measurement of a self-amplified free-electron laser. *Phys. Rev. Lett.* **89**, 234801 (2002).
55. Emma, P. et al. Femtosecond and Subfemtosecond X-Ray Pulses from a SASE Based Free-Electron Laser. *Phys. Rev. Lett.* **92**, 074801 (2004).
56. Helml, W. et al. Ultrashort free-electron laser X-ray pulses. *Appl. Sci.* **7**, 915–956 (2017).

Acknowledgements

Author contributions

N.H., M.I., A.O.L., R.N.C. and W.H. conceived and coordinated the experiment. N.H., R.H., M.S.W., C.B., J.L., A.A.M., S.P.M., J.R., R.N.C. and W.H. built the vacuum system and the optical set-up, and supervised them during the measurement. M.I, J.B., A.O.L., J.G., M.P. and J.V. were responsible for constructing, installing and operating the photoelectron detector. J.K., A.A.L. and A.M. and T.M. carried out accelerator control and

XFEL characterization. N.H., G.H., R.H., M.S.W., J.B., A.O.L., J.L., R.N.C. and W.H. performed data analysis. N.H., G.H., M.I., T.F., R.K., R.N.C. and W.H. interpreted data and oversaw manuscript production. A.K.K., N.M.K. and T.F. provided simulations for comparison with experimental data. N.H., G.H. and W.H. wrote the paper with extensive contributions from all authors.

Competing interests

The authors declare no competing interests.

Additional information

Supplementary information is available for this paper at https://doi.org/10.1038/s41566-018-0107-6.

Reprints and permissions information is available at www.nature.com/reprints.

Correspondence and requests for materials should be addressed to N.H. or W.H.

Publisher's note: Springer Nature remains neutral with regard to jurisdictional claims in published maps and institutional affiliations.

Methods

FEL machine parameters. The FEL was run at 120 Hz, with a mean bunch charge of 150 pC, average electron beam energy of 5,087 MeV and a mean peak current of 1,500 A. The electron bunch length was about 85 fs, but the effective lasing part is considerably shorter because of the emittance spoiler[55]. The generated X-ray pulses have an average pulse energy of 64 μJ with a standard deviation of ±15 μJ at a mean photon energy of 1,180 eV, corresponding to 3.4×10^{11} photons per pulse (compare Supplementary Fig. 1a), and a mean spectral bandwidth of 7.1 eV (FWHM).

Optical set-up. The optical set-up consists of an ultrafast Ti:sapphire amplifier system (800 nm, 30 mJ, 100 fs, 120 Hz) and an optical parametric amplifier (OPA). The 800 nm input is converted to 10.6 μm via difference frequency generation of signal and idler in the commercial OPA system, generating 340 fs FWHM pulses with an average pulse energy of 38 μJ (see Supplementary Fig. 1b for the distribution of the IR single-shot pulse energies). A reflective phase retarder commonly used for CO_2 lasers converts the linear polarization of the OPA output to close-to-circular polarization with an ellipticity $\varepsilon = 0.73 \pm 0.03$, measured as the ratio of the two half-axes of the polarization ellipse, with a tilt of $22.5° \pm 5°$ of the major half-axis with respect to the vertical detector orientation. Since the stability of the ellipticity is directly related to the inherently stable original linear polarization of the OPA and the set-up for conversion from linear to elliptical polarization was relying only on one fixed reflective optic, the ellipticity is stable within the measurement error during the experiment. A ZnSe lens of 150 mm focal length, positioned directly in front of the KBr incoupling window, focused the mid-infrared beam to a spot size of 500 μm ($1/e^2$ diameter) in the interaction region.

Time-of-flight spectrometer and data acquisition. The instrument consists of 16 independent TOF electron spectrometers located in steps of 22.5° in a plane perpendicular to the beam axis. Their respective acceptance volumes overlap with each other and the XFEL beam, allowing for the simultaneous observation of photoemission spectra at 16 angles in discrete steps over a full circle. The XFEL pulses are focused to a spot size of approximately 50 μm diameter ($1/e^2$) in the spectrometers' common acceptance volume, which is filled with neon gas at an ambient pressure of 4.4×10^{-6} mbar. The angular acceptance of each flight tube depends on its configurable deceleration voltage of a few to thousands of volts and has an upper limit of 3.8×10^{-2} sr (corresponding to a full opening angle of 12.6° from the beam position), determined by the diameter of its entrance aperture. The detector unit uses a stack of three multi-channel plate (MCP) amplifiers with capacitive outcoupling of the area-integrated signal. The signal is processed via Acqiris DC282 digitizers operated in interleaved mode at 4 GS s^{-1} (non-interleaved 2 GS s^{-1}). The pulse duration of the single-electron response of the MCP detector amounts to ~1 ns (FWHM), which is not significantly broadened by the subsequent signal amplification and data processing. Since the time of flight of each incoming electron is strictly related to its kinetic energy, the energy resolution of the method is directly connected to the acquired time/energy window as well as the resolvable pulse width. Our streaking signal was typically spread over approximately 50 ns. Several hundreds of hits in the chosen energy window can be acquired during this time without leaving the linear amplification regime, which is a precondition for single-shot spectroscopy. Accordingly, the measured voltage through the MCPs reflects the number of detected photoelectrons per unit time recorded in each channel (that is, 0.25 ns in interleaved digitizer operation). Hence, the energy resolution of the individual time-of-flight detectors depends on the actual time of flight of the recorded electrons—and is worse for shorter flight times and thus for high-energy electrons. The experimentally determined resolution amounts to better than 0.75 eV to 1 eV for the highest-energy electrons under the applied measurement conditions.

Data availability. The data that support the plots within this paper and other findings of this study are available from the corresponding authors upon reasonable request. The raw data of all the described measurements are also stored in the dedicated data repository at LCLS/SLAC.